JOURNAL OF SPACECRAFT AND ROCKETS
Vol. 44, No. 3, May–June 2007

Numerical Studies of Magnetohydrodynamic Flow Control Considering Real Wall Electrical Conductivity

Takayasu Fujino,* Yusuke Matsumoto,† Jiro Kasahara,* and Motoo Ishikawa‡
University of Tsukuba, Tsukuba 305-8573, Japan

DOI: 10.2514/1.25824

Effectiveness of the magnetohydrodynamic (MHD) flow control is explored, where effects of electrical conductivity of wall of a space vehicle are studied by two-dimensional numerical simulations under the reentry flight conditions at the altitude of about 60 km in the OREX experiment (in Japan, 1994) for a wide range of the electrical conductivity of wall (from 10^{-5} to 10^{5} S/m) and for three different values of the wall thickness: 1, 10, and 100 mm. The computational code employs Park's two-temperature model, Dunn and Kang's chemical reactions model, and the low magnetic Reynolds number model with the Hall effect. The numerical results clearly show that there is an upper limit of the electrical conductivity of wall for making the MHD flow control useful. When the electrical conductivity of wall is the value of upper limit or less, the difference in the electrical conductivity does not influence the effectiveness of the MHD flow control.

Nomenclature

$\boldsymbol{B}$	=	magnetic field vector
B_r, B_z	=	components of magnetic flux density in the r- and z-directions
B_0	=	magnetic flux density at stagnation point
D_s	=	effective diffusion coefficient of species s
$\hat{D}_s$	=	average vibrational energy of molecule s, which is created or destroyed at rate $\dot{\omega}_s$
E	=	total energy
$\boldsymbol{E}$	=	electric field vector
E_r, E_z	=	components of electric field in the r- and z-directions
e	=	electronic charge
$\boldsymbol{e_r}$, $\boldsymbol{e_z}$	=	unit vectors in r- and z-directions
$e_{\mathrm{ve},s}$	=	vibrational-electronic-electron energy of species s
$e^*_{v,s}$	=	equilibrium vibrational energy of species s
H	=	total enthalpy
h_s	=	enthalpy of species s
$h_{\mathrm{ve},s}$	=	vibrational-electronic-electron enthalpy of species s
I_s	=	first ionization energy of species s
$\boldsymbol{J}$	=	vector of electric current density
J_r, J_θ, J_z	=	components of electric current density in the r-, θ-, and z-directions
k_b	=	Boltzmann's constant
$k_{f,r}$, $k_{b,r}$	=	forward and backward reaction rate coefficients for reaction r
M_e	=	molecular weight of electron
M_s	=	molecular weight of species s
m_e	=	mass of electron
n_e	=	electron number density
$\dot{n}_{e,s}$	=	molar rate of production of species s by electron impact ionization
p	=	static pressure
p_e	=	electron partial pressure
p_s	=	partial pressure of species s
R	=	universal gas constant
R_b	=	nose radius of body
$R_{f,r}$, $R_{b,r}$	=	forward and backward reaction rates for reaction r
r, θ, z	=	cylindrical coordinates
T_{tr}	=	translational-rotational temperature
T_{ve}	=	vibrational-electronic-electron temperature
t	=	time
u_r, u_θ, u_z	=	velocity components in the r-, θ-, and z-directions
y_s	=	mole fraction of species s
$\alpha_{s,r}$, $\beta_{s,r}$	=	forward and backward stoichiometric coefficients of species s in reaction r
β	=	electron Hall parameter in gas
Δ_{wall}	=	thickness of wall with electrical conductivity
ϵ_0	=	permittivity of vacuum
η_{tr}	=	mixture translational-rotational thermal conductivity
η_{ve}	=	mixture vibrational-electron thermal conductivity
μ	=	mixture viscosity
$\nu_{e,s}$	=	effective energy exchange collision frequency of electron with species s
$\nu^m_{e,s}$	=	effective momentum transfer collision frequency of electron with species s
ξ, η	=	generalized curvilinear coordinates
ρ	=	total mass density
ρ_s	=	mass density of species s
σ_{gas}	=	electrical conductivity in gas
$\sigma^m_{e,s}$	=	effective momentum transfer cross section of electrons with neutral species s
σ_{wall}	=	electrical conductivity in wall
$\tau_{i,j}$	=	viscous shear stress
τ_s	=	translational-vibrational energy relaxation time of species s
ϕ	=	electric potential
ω_s	=	mass production rate of species s
$\dot{\omega}_{\mathrm{ve}}$	=	production rate of vibrational-electronic-electron energy

Presented as Paper 2891 at the 37th AIAA Plasmadynamics and Lasers Conference, San Francisco, CA, 5–8 June 2006; received 13 June 2006; revision received 12 October 2006; accepted for publication 17 October 2006.

*Assistant Professor, Graduate School of Systems and Information Engineering. Member AIAA.
†Graduate Student, Graduate School of Systems and Information Engineering.
‡Professor, Graduate School of Systems and Information Engineering. Senior Member AIAA.

I. Introduction

AS ONE of active thermal protection techniques in earth-reentry flights, a flow control using magnetohydrodynamic (MHD) technology, which is called the MHD flow control, has been proposed in the 1950s (for example, see [1–3]). The idea of the MHD flow control is that the Lorentz force, which is induced by applying

the magnetic field to the weakly ionized plasma flow in the shock layer, decelerates the flow velocity in the shock layer and pushes the bow shock wave away from a space vehicle. Consequently, the convective aerodynamic heating can be reduced by the MHD flow control. In the 1950s, the concept of the MHD flow control was not considered to be realistic because a very large and heavy magnet system was required to produce the strong magnetic field enough to control the flow in the shock layer. However, a considerable development of magnet technology with a superconducting magnet has been shown in more than a half century since the concept of the MHD flow control was proposed. The considerable development of the magnet system technology encourages us to reconsider the MHD flow control.

The authors conducted a numerical study [4] for examining the possibility and usefulness of the MHD flow control under the real earth-reentry flight conditions at the altitude of about 60 km in the OREX experiment [5] (in Japan, 1994). The blunt body OREX has the nose radius of 1.35 m and the axisymmetric two-dimensional (r–z) shape. For the numerical study, the authors developed a two-dimensional computational code, which can consider the thermochemical nonequilibrium state and the Hall effect in the MHD flow. Results of the numerical study have indicated that the electrical conductivity of the thermal protection wall touched with the flow considerably influences the MHD flow control. In the case of the wall without any electrical conductivity, applying a dipole-type applied magnetic filed with r- and z-components can push the bow shock wave and reduce the aerodynamic heating. On the other hand, in the case of the wall with infinite electrical conductivity, the strong Hall electric field cannot be induced owing to the existence of the path of electric current between plasma flows and wall, so that a large azimuthal electric current cannot be obtained. As a result, the shock wave, in this case, cannot be pushed away from the body and the aerodynamic heating cannot be reduced.

The numerical study, however, treated the electrical conductivity of the wall as zero or infinity. Practically, the wall has a finite electrical conductivity. The present study, therefore, conducts two-dimensional numerical simulations of the MHD flow control under the flight conditions at the altitude of about 60 km of OREX for a wide range of the electrical conductivity of wall: from 10^{-5} to 10^{5} S/m to clarify the upper limit of the electrical conductivity of wall material for making the MHD flow control useful. We can confidently expect that the upper limit depends on the thickness of the wall. And so the present numerical simulations are carried out for three different values of the wall thickness: 1, 10, and 100 mm.

II. Numerical Method and Numerical Condition

A. Flight Conditions and Applied Magnetic Field

Figure 1 shows the configuration of OREX [5]. The forebody shape is composed of a spherical nose with a radius of 1.35 m, a cone, and a circular shoulder. Numerical flight conditions correspond to the OREX flight conditions at the altitude of 59.6 km, where the aerodynamic heating was maximum in the OREX experiment. The

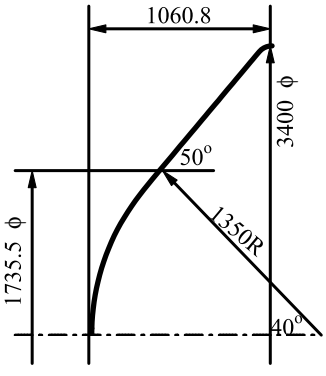

Fig. 1 OREX configuration (unit: millimeters).

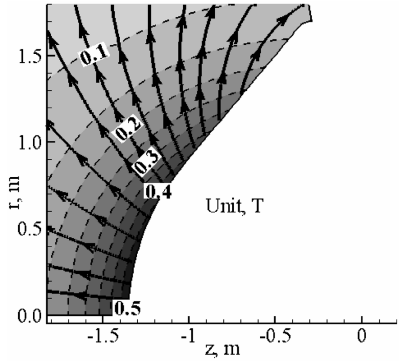

Fig. 2 Distribution of applied magnetic field ahead of OREX.

freestream velocity is 5562 m/s, the freestream pressure 23.6 Pa, and the freestream temperature 248.1 K.

Figure 2 shows an externally applied magnetic field ahead of OREX. The externally applied magnetic field is assumed to be produced by a dipole magnet placed at the point of $r = 0$ m and $z = 0$ m inside OREX:

$$\boldsymbol{B}(r,z) = -\frac{B_0 R_b^3}{2(z^2+r^2)^{3/2}}\left[\left(\frac{2z^2}{z^2+r^2}-\frac{r^2}{z^2+r^2}\right)\boldsymbol{e}_z + \frac{3zr}{z^2+r^2}\boldsymbol{e}_r\right] \tag{1}$$

In the present study, B_0 is set to 0.5 T.

B. Basic Equations

We regard the flowfield and the electromagnetic field as axisymmetric two-dimensional field (r–z).

1. Gasdynamics

The basic equations for the gasdynamics are the mass conservation equations of chemical species, the momentum conservation equations, the total energy conservation equation, and the vibrational-electronic-electron energy conservation equation. We consider the following 11 chemical species: N, O, N_2, O_2, NO, N^+, O^+, N_2^+, O_2^+, NO^+, and e^-. As a finite rate chemical kinetics model, we use Dunn and Kang's model [6], in which 32 chemical reactions are included. Park's two-temperature model [7] is employed to take account of the thermal nonequilibrium state. The basic equations for the gasdynamics are written as follows:

Mass conservation equations of chemical species (s = N, O, N_2, O_2, NO, N^+, O^+, N_2^+, O_2^+, NO^+, e^-):

$$\frac{\partial \rho_s}{\partial t} + \frac{\partial}{\partial r}(\rho_s u_r) + \frac{\partial}{\partial z}(\rho_s u_z) = \dot{\omega}_s + \frac{\partial}{\partial r}\left(\rho D_s \frac{\partial y_s}{\partial r}\right) + \frac{\partial}{\partial z}\left(\rho D_s \frac{\partial y_s}{\partial z}\right) - \frac{1}{r}\left(\rho_s u_r - \rho D_s \frac{\partial y_s}{\partial r}\right) \tag{2}$$

where the total mass density is given by

$$\rho = \sum_s \rho_s \tag{3}$$

The first term $\dot{\omega}_s$ on the right-hand side of Eq. (2) is the source term for the mass production rate of species s, and is expressed as

$$\dot{\omega}_s = M_s \sum_{r=1}^{32} (\beta_{s,r} - \alpha_{s,r})(R_{f,r} - R_{b,r}) \tag{4}$$

The forward and backward reaction rates are, respectively, defined by

$$R_{f,r} = k_{f,r} \prod_{s=1}^{11} (\rho_s / M_s)^{\alpha_{s,r}}, \qquad R_{b,r} = k_{b,r} \prod_{s=1}^{11} (\rho_s / M_s)^{\beta_{s,r}} \tag{5}$$

where the forward reaction rate coefficients and the backward reaction rate coefficients are tabulated in [6,8].

Momentum conservation equations:

$$\frac{\partial \rho u_r}{\partial t} + \frac{\partial}{\partial r}\left(\rho u_r^2 + p\right) + \frac{\partial}{\partial z}(\rho u_r u_z) = \frac{\partial \tau_{rr}}{\partial r} + \frac{\partial \tau_{rz}}{\partial z} + J_\theta B_z - \frac{1}{r}\left[\rho\left(u_r^2 - u_\theta^2\right) - \tau_{rr} + \tau_{\theta\theta}\right] \tag{6}$$

$$\frac{\partial \rho u_\theta}{\partial t} + \frac{\partial}{\partial r}(\rho u_\theta u_r) + \frac{\partial}{\partial z}(\rho u_\theta u_z) = \frac{\partial \tau_{r\theta}}{\partial r} + \frac{\partial \tau_{z\theta}}{\partial z} + J_z B_r - J_r B_z - \frac{2}{r}(\rho u_r u_\theta - \tau_{r\theta}) \tag{7}$$

$$\frac{\partial \rho u_z}{\partial t} + \frac{\partial}{\partial r}(\rho u_z u_r) + \frac{\partial}{\partial z}\left(\rho u_z^2 + p\right) = \frac{\partial \tau_{rz}}{\partial r} + \frac{\partial \tau_{zz}}{\partial z} - J_\theta B_r - \frac{1}{r}(\rho u_r u_z - \tau_{rz}) \tag{8}$$

where the static pressure and the viscous stress terms are defined by

$$p = \sum_s p_s = \sum_{s=1-10} \rho_s \frac{\bar{R}}{M_s} T_{\mathrm{tr}} + \rho_e \frac{\bar{R}}{M_e} T_{\mathrm{ve}} \tag{9}$$

$$\tau_{rr} = \frac{2}{3}\mu\left(2\frac{\partial u_r}{\partial r} - \frac{\partial u_z}{\partial z} - \frac{u_r}{r}\right), \quad \tau_{\theta\theta} = \frac{2}{3}\mu\left(2\frac{u_r}{r} - \frac{\partial u_r}{\partial r} - \frac{\partial u_z}{\partial z}\right)$$
$$\tau_{zz} = \frac{2}{3}\mu\left(2\frac{\partial u_z}{\partial z} - \frac{\partial u_r}{\partial r} - \frac{u_r}{r}\right), \quad \tau_{r\theta} = \tau_{\theta r} = \mu\left(\frac{\partial u_\theta}{\partial r} - \frac{u_\theta}{r}\right)$$
$$\tau_{rz} = \tau_{zr} = \mu\left(\frac{\partial u_r}{\partial z} + \frac{\partial u_z}{\partial r}\right), \quad \tau_{\theta z} = \tau_{z\theta} = \mu\frac{\partial u_\theta}{\partial z} \tag{10}$$

Total energy conservation equation:

$$\begin{aligned}\frac{\partial \rho E}{\partial t} + \frac{\partial}{\partial r}(\rho H u_r) + \frac{\partial}{\partial z}(\rho H u_z) &= \frac{\partial}{\partial r}\left(\eta_{\mathrm{tr}}\frac{\partial T_{\mathrm{tr}}}{\partial r} + \eta_{\mathrm{ve}}\frac{\partial T_{\mathrm{ve}}}{\partial r}\right) + \frac{\partial}{\partial z}\left(\eta_{\mathrm{tr}}\frac{\partial T_{\mathrm{tr}}}{\partial z} + \eta_{\mathrm{ve}}\frac{\partial T_{\mathrm{ve}}}{\partial z}\right) + \frac{\partial}{\partial r}\left(\rho\sum_s h_s D_s \frac{\partial y_s}{\partial r}\right) \\ &+ \frac{\partial}{\partial z}\left(\rho\sum_s h_s D_s \frac{\partial y_s}{\partial z}\right) + \frac{\partial}{\partial r}(\tau_{rr}u_r + \tau_{\theta r}u_\theta + \tau_{zr}u_z) \\ &+ \frac{\partial}{\partial z}(\tau_{rz}u_r + \tau_{\theta z}u_\theta + \tau_{zz}u_z) + J_r E_r + J_z E_z - \frac{\rho H u_r}{r} \\ &+ \frac{\rho}{r}\sum_s h_s D_s \frac{\partial y_s}{\partial r} + \frac{1}{r}\left(\eta_{\mathrm{tr}}\frac{\partial T_{\mathrm{tr}}}{\partial r} + \eta_{\mathrm{ve}}\frac{\partial T_{\mathrm{ve}}}{\partial r}\right) \\ &+ \frac{1}{r}(\tau_{rr}u_r + \tau_{\theta r}u_\theta + \tau_{zr}u_z)\end{aligned} \tag{11}$$

where the total enthalpy is defined as

$$H = E + \frac{p}{\rho} \tag{12}$$

Vibrational-electronic-electron energy conservation equation:

$$\begin{aligned}\frac{\partial \rho e_{\mathrm{ve}}}{\partial t} + \frac{\partial}{\partial r}(\rho e_{\mathrm{ve}} u_r) + \frac{\partial}{\partial z}(\rho e_{\mathrm{ve}} u_z) &= \dot{\omega}_{\mathrm{ve}} + \frac{\partial}{\partial r}\left(\eta_{\mathrm{ve}}\frac{\partial T_{\mathrm{ve}}}{\partial r}\right) + \frac{\partial}{\partial z}\left(\eta_{\mathrm{ve}}\frac{\partial T_{\mathrm{ve}}}{\partial z}\right) + \frac{\partial}{\partial r}\left(\rho\sum_s h_{\mathrm{ve},s} D_s \frac{\partial y_s}{\partial r}\right) \\ &+ \frac{\partial}{\partial z}\left(\rho\sum_s h_{\mathrm{ve},s} D_s \frac{\partial y_s}{\partial z}\right) + \frac{J_r^2 + J_\theta^2 + J_z^2}{\sigma_{\mathrm{gas}}} \\ &- \frac{1}{r}\left(\rho e_{\mathrm{ve}} u_r - \rho\sum_s h_{\mathrm{ve},s} D_s \frac{\partial y_s}{\partial r} - \eta_{\mathrm{ve}}\frac{\partial T_{\mathrm{ve}}}{\partial r}\right)\end{aligned} \tag{13}$$

where $\dot{\omega}_{\mathrm{ve}}$ is expressed as

$$\dot{\omega}_{\mathrm{ve}} = \sum_{s=\mathrm{mol}} \rho_s \frac{e_{v,s}^* - e_{v,s}}{\langle \tau_s \rangle} + 2\rho\frac{3}{2}\bar{R}(T_{\mathrm{tr}} - T_{\mathrm{ve}})\sum_{s\neq e}\frac{\nu_{e,s}}{M_s} - \sum_{s=\mathrm{ion}} \dot{n}_{e,s} I_s + \sum_{s=\mathrm{mol}} \dot{\omega}_s \hat{D}_s - p_e\left(\frac{\partial u_r}{\partial r} + \frac{\partial u_z}{\partial z} + \frac{u_r}{r}\right) \tag{14}$$

where the relaxation time τ_s of each species for a translational-vibrational energy relaxation is calculated from the sum of the relaxation time formula proposed by Millikan and White [9] and the correction term suggested by Park [7]. The effective energy exchange frequency of electrons with other species is estimated by following [8]. The average vibrational energy $\hat{D}_s$, which is created or destroyed at the rate $\dot{\omega}_s$, is computed by using the nonpreferential model [8]. The transport coefficients such as the effective diffusion coefficient of each species, the mixture viscosity, the mixture translational-rotational thermal conductivity, and the mixture vibrational-electron thermal conductivity are estimated by an extension model of Yos' formulas to the multitemperature gas mixture (see [8]).

2. *Electrodynamics*

The basic equations used for the electrodynamics both in the flowfield and in the wall are the steady Maxwell equations and the generalized Ohm's law. The magnetic Reynolds number is less than unity under the present numerical conditions, and then we neglect the induced magnetic field. The basic equations for the electrodynamics are written as follows:

Maxwell equations:

$$\nabla \times \boldsymbol{E} = 0 \tag{15}$$

$$\nabla \cdot \boldsymbol{J} = 0 \tag{16}$$

Generalized Ohm's law in gas:

$$\begin{pmatrix} J_r \\ J_\theta \\ J_z \end{pmatrix} = \frac{\sigma_{\mathrm{gas}}}{1+\beta^2} \times \begin{pmatrix} 1 + m^2 B_r^2 & -mB_z & m^2 B_r B_z \\ mB_z & 1 & -mB_r \\ m^2 B_r B_z & mB_r & 1 + m^2 B_z^2 \end{pmatrix} \begin{pmatrix} E_r + u_\theta B_z + \frac{1}{en_e}\frac{\partial p_e}{\partial r} \\ u_z B_r - u_r B_z \\ E_z - u_\theta B_r + \frac{1}{en_e}\frac{\partial p_e}{\partial z} \end{pmatrix}, \quad m = \beta/|\boldsymbol{B}| \tag{17}$$

Ohm's law in wall:

$$\begin{pmatrix} J_r \\ J_\theta \\ J_z \end{pmatrix} = \sigma_{\mathrm{wall}} \begin{pmatrix} E_r \\ 0 \\ E_z \end{pmatrix} \tag{18}$$

The electrical conductivity and the Hall parameter in gas are, respectively, expressed as

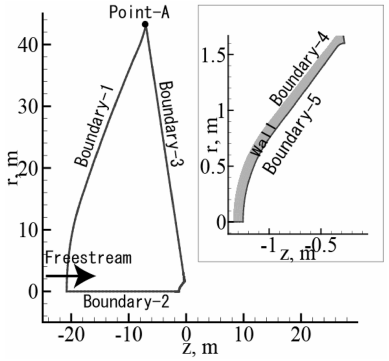

Fig. 3 Computational region.

$$\sigma_{\text{gas}} = \frac{n_e e^2}{m_e \sum_{s \neq e} \nu_{e,s}^m}, \qquad \beta = \frac{e|\boldsymbol{B}|}{m_e \sum_{s \neq e} \nu_{e,s}^m} \tag{19}$$

The effective momentum transfer collision frequency of electrons with the other chemical species is written as

$$\nu_{e,s}^m = \begin{cases} 6\pi \left(\frac{e^2}{12\pi\epsilon_0 k_b T_{\text{ve}}} \right)^2 \ell_n \left[12\pi \left(\frac{\epsilon_0 k_b}{e^2} \right)^{3/2} \sqrt{\frac{T_{\text{ve}}^3}{n_e}} \right] n_s \sqrt{\frac{8 k_b T_{\text{ve}}}{\pi m_e}} & \text{if } s \text{ is ion species} \\ \frac{4}{3} \sigma_{e,s}^m n_s \sqrt{\frac{8 k_b T_{\text{ve}}}{\pi m_e}} & \text{otherwise} \end{cases} \tag{20}$$

where $\sigma_{e,s}^m$ is computed using the curve fit presented in [8]. The electrical conductivity in the wall, which is a numerical parameter in the present study, is set to be a value in a wide range from 10^{-5} to 10^5 S/m. The wall is assumed to be nonmagnetic and nonmagnetized in the present numerical simulation.

In the present study, the ion slip term in the generalized Ohm's law is neglected for simplicity. As shown in the section of Results and Discussion, the electron Hall parameter is about 10–15 in the shock layer. From the value of the electron Hall parameter, the ion Hall parameter is estimated at the order of 0.1, and so the product of electron and ion Hall parameters, which is estimated at the order of 1. The absolute value of the ratio of the ion slip term to the Hall-effect term in the generalized Ohm's law is estimated at the order of 0.1. We, therefore, think that the ion slip phenomenon does not make considerable differences from the numerical results obtained in the present study, where the ion slip effect is neglected.

C. Numerical Procedure

A computational region is shown in Fig. 3. The computational region of the flowfield is the region surrounded by the boundary lines 1, 2, 3, and 4 in Fig. 3. The computational region of electrodynamics is the region surrounded by the boundary lines 1, 2, 3, and 5. The region between the boundary line 4 and the boundary line 5 corresponds to the wall with the electrical conductivity σ_{wall} and the thickness Δ_{wall}. The number of grid points in the flowfield is 65 in the ξ-direction along the wall surface and 250 in the outward η-direction. Because the prediction of the heat flux on the wall surface is extremely sensitive to the grid near the wall surface, we checked the grid dependency in advance. Based on the check, we set the minimum mesh size near the wall surface to about 2 μm. The number of grid points in the wall is 65 in the ξ-direction and 10 in the η-direction.

The conservation equations of the gasdynamics are transformed into the generalized coordinate system. The convection terms are calculated by the advection upstream splitting method (AUSM)-DV [10] coupled with the fourth-order compact MUSCL TVD scheme [11]. The viscous terms are calculated by the second-order central-differencing scheme. The time integration is performed by the lower-upper symmetric Gauss–Seidel (LU-SGS) scheme [12].

The boundary conditions for the gasdynamics are specified as follows:

Inflow (the boundary line 1 in Fig. 3): Freestream conditions, which correspond to the flight conditions at the altitude of 59.6 km in the OREX experiment are given as

$$\frac{\rho_{\text{N}_2}}{\rho} = 0.79, \qquad \frac{\rho_{\text{O}_2}}{\rho} = 0.21, \qquad u_z = 5562 \text{ m/s}$$
$$u_r = u_\theta = 0.0 \text{ m/s} \qquad p = 23.6 \text{ Pa}, \qquad T_{\text{tr}} = T_{\text{ve}} = 248.1 \text{ K}$$

Outflow (the boundary line 3 in Fig. 3): Zero-order extrapolation is used for all primitive variables ($\rho_s, u_r, u_\theta, u_z, p, T_{\text{tr}}, T_{\text{ve}}$).

Symmetric line (the boundary line 2 in Fig. 3): u_r and u_θ are set to zero, and the normal gradient is set to zero for the other primitive variables ($\rho_s, u_z, p, T_{\text{tr}}, T_{\text{ve}}$).

Wall surface (the boundary line 4 in Fig. 3): The no-slip wall condition, the fixed wall temperature condition, and the noncatalytic wall condition are used, and the translational-rotational temperature and the vibrational-electronic-electron temperature on the wall surface are assumed to be equilibrium with the wall temperature. The wall temperature is set to 1519 K; this value corresponds to the wall temperature at the stagnation point estimated at the altitude of 59.6 km in the OREX experiments.

$$\frac{\partial \rho_s}{\partial n} = 0, \qquad u_z = u_r = u_\theta = 0.0 \text{ m/s}$$
$$T_{\text{tr}} = T_{\text{ve}} = T_{\text{wall}} = 1519 \text{ K}$$

We derive a second-order elliptic partial differential equation on the electric potential from Eqs. (15–18). The equation is solved by the Galerkin finite element method (FEM) under the following boundary conditions: the normal component of electric current density J_n on the boundary lines 1, 2, 3, and 5 in Fig. 3 is set to 0 A/m^2, whereas the electric potential at the point A in Fig. 3 is set to 0 V for establishing a reference value of electric potential.

As shown in [13], we compared shock location of both numerical results and experimental data in Lobb's experiments [14] to validate the reliability of the numerical solutions as for the gasdynamics part. As a result, good agreement between numerical results and experimental data was obtained. We also confirmed by comparing the numerical results and experimental data in MHD power generation experiments with a large-scale generator "Sakhalin" that the reliability of the numerical solutions as for the electrodynamics part is very high [15].

III. Results and Discussion

First, numerical results in the case of the wall thickness of 100 mm will be described to facilitate understanding of the interaction between the MHD flow and the wall with electrical conductivity. And then, the influence of the thickness of wall with electrical conductivity on the upper limit will be briefly discussed with numerical results in the cases of the wall thickness of 1 and 10 mm, as well as 100 mm.

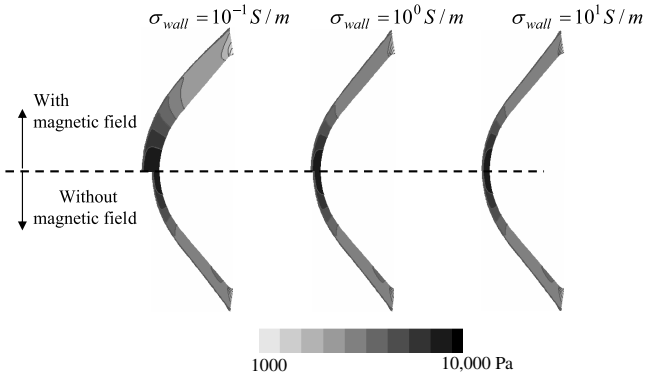

Fig. 4 Distributions of static pressure ahead of body (Δ_{wall}= 100 mm).

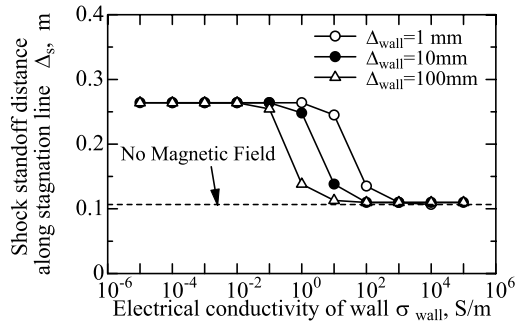

a)

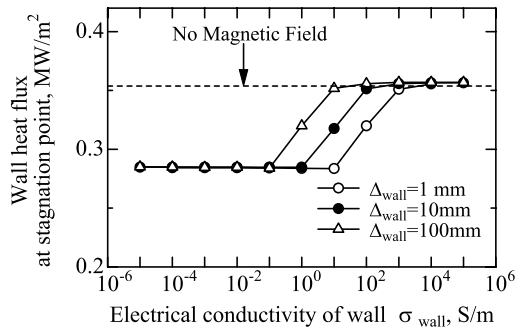

b)

Fig. 5 a) Shock standoff distance along the stagnation line and b) wall heat flux at the stagnation point.

Figure 4 depicts two-dimensional distributions of the static pressure ahead of the body with applying the magnetic field for the electrical conductivity of wall of 10^{-1}, 10^{0}, and 10^{1} S/m when the wall thickness is 100 mm. The distribution of the static pressure without applying the magnetic field is also illustrated in Fig. 4. For the electrical conductivity of wall of 10^{-1} S/m, the shock wave is pushed away from the body by applying the magnetic field. On the other hand, the increase of shock standoff distance by applying magnetic field is too slight to be noticed for the electrical conductivity of wall of 10^{0} S/m, and the shock standoff distance cannot be increased at all by applying the magnetic field for the electrical conductivity of wall of 10^{1} S/m.

Figure 5a illustrates the shock standoff distance along the stagnation line and Fig. 5b illustrates the wall heat flux at the stagnation point for a wide range of the electrical conductivity of wall (from 10^{-5} to 10^{5} S/m) and for three different values of wall thickness: 1, 10, and 100 mm. When the electrical conductivity of wall is 10^{-1} S/m or less and the wall thickness is 100 mm, the shock standoff distance can be increased and the wall heat flux can be reduced by applying the magnetic field, and also these values do not significantly vary with respect to the value of electrical conductivity of wall. The wall heat flux in the case of the wall electrical conductivity of 10^{-1} S/m or less is reduced to about 70% of its value without applying the magnetic field. We can also confirm from Fig. 5 that the increase of shock standoff distance and the reduction of wall heat flux by applying the magnetic field decrease with increasing of the electrical conductivity from 10^{-1} to 10^{1} S/m. When the electrical conductivity of wall is more than 10^{1} S/m, the shock standoff distance cannot be increased and the wall heat flux cannot be reduced by applying the magnetic field. And thus, Fig. 5 shows that there is an upper limit of the electrical conductivity of wall for making the MHD flow control useful, and the upper limit in the case of wall thickness of 100 mm is 10^{-1} S/m under the present flight conditions.

Figure 6 illustrates two-dimensional distributions of the azimuthal electric current density for the electrical conductivity of wall of 10^{-2}, 10^{-1}, 10^{0}, and 10^{1} S/m in the case of the wall thickness of 100 mm. The Lorentz force generated by the interaction between the azimuthal electric current density and the applied magnetic field decelerates the flow in the shock layer and pushes the bow shock wave. The distribution of the azimuthal electric current density for the electrical conductivity of wall of 10^{-2} S/m is almost the same as that for the electrical conductivity of wall of 10^{-1} S/m, which corresponds to the upper limit of the electrical conductivity of wall for making the MHD flow control useful. Although figures are omitted because of space limitation, distributions of the azimuthal electric current density for the electrical conductivity of wall of 10^{-1} or less are almost the same. The increase of shock standoff distance by applying the magnetic field, therefore, does not vary with respect to the value of electrical conductivity of wall of 10^{-1} S/m or less. As shown in Fig. 6, the magnitude of azimuthal electric current density significantly reduces as the electrical conductivity of wall increases from 10^{-1} to 10^{1} S/m, so that the increase of the shock standoff distance by applying the magnetic field decreases with increasing of the electrical conductivity, as shown in Figs. 4 and 5. For the electrical conductivity of wall more than 10^{1} S/m where the shock standoff distance cannot be increased at all by applying the magnetic field, the maximum value of azimuthal electric current density is less than one-tenth of that for the electrical conductivity of wall of 10^{-1} S/m.

Figure 7a depicts the electrical conductivity and Fig. 7b depicts the Hall parameter in gas along the stagnation line for the electrical conductivity of wall of 10^{-2}, 10^{-1}, 10^{0}, and 10^{1} S/m in the case of the wall thickness Δ_{wall} of 100 mm. For any electrical conductivity of wall, the electrical conductivity in gas is about 115 S/m behind the bow shock wave, and then it decreases from about 115 to 0 S/m toward the stagnation point. The Hall parameter is about 10–15 in the shock layer for any electrical conductivity of wall. Thus, the difference of the magnitudes of azimuthal electric current density for the electrical conductivity of wall of 10^{-1}, 10^{0}, and 10^{1} S/m has nothing to do with the effective electrical conductivity in gas $\sigma_{gas}/(1+\beta^2)$.

The Hall parameter in the shock layer, as has been mentioned, is about 10–15 for any electrical conductivity of wall. This fact indicates that the characteristics of electric field and electric current in the flowfield are dominated by the Hall effect. The difference of electric potential on the r–z plane, that is, the electric field with r- and z-components is induced by the Hall effect. As the difference of electric potential in the direction of flow along the wall becomes larger, the azimuthal electric current density increases larger.

As shown in Fig. 8, the difference of the electric potential between the stagnation point and the shoulder of the body is about 4000 V for the electrical conductivity of wall of 10^{-1} S/m or less, where the shock wave can be pushed away from the body by applying the magnetic field. The difference of the electric potential between the stagnation point and the shoulder of the body decreases as the electrical conductivity of wall increases from 10^{-1} to 10^{1} S/m. The difference of the electric potential between the stagnation point and the shoulder of the body for the electrical conductivity of wall of 10^{1} S/m is less than one-tenth of that for the electrical conductivity of wall of 10^{-1} S/m. Although figures are omitted because of space limitation, the distributions of electric potential for the electrical conductivity of wall more than 10^{1} S/m are almost the same. Consequently, the azimuthal electric current density with the

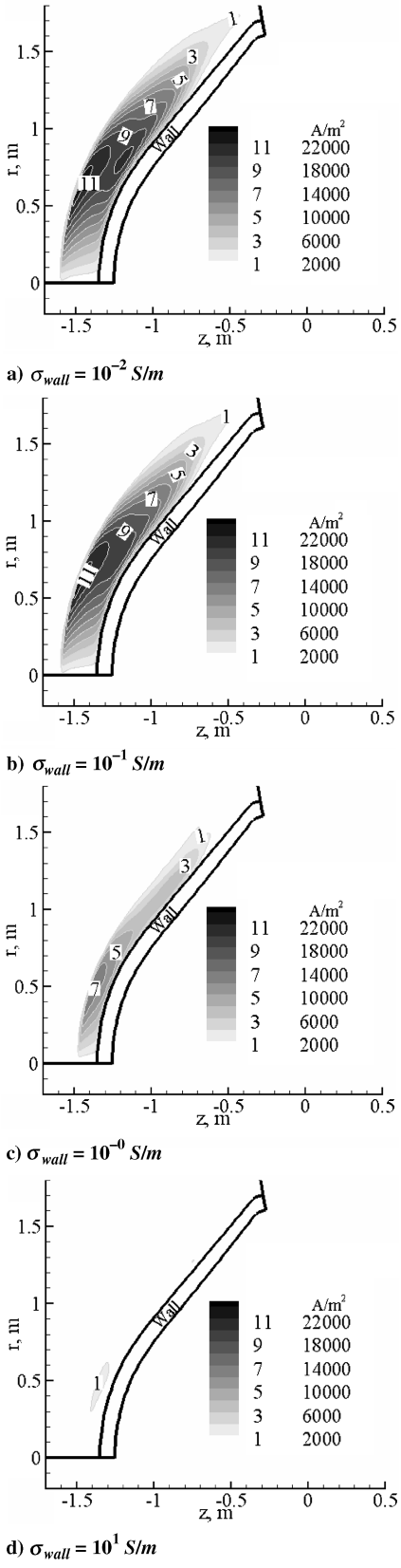

Fig. 6 Distributions of azimuthal electric current density (Δ_{wall}= 100 mm).

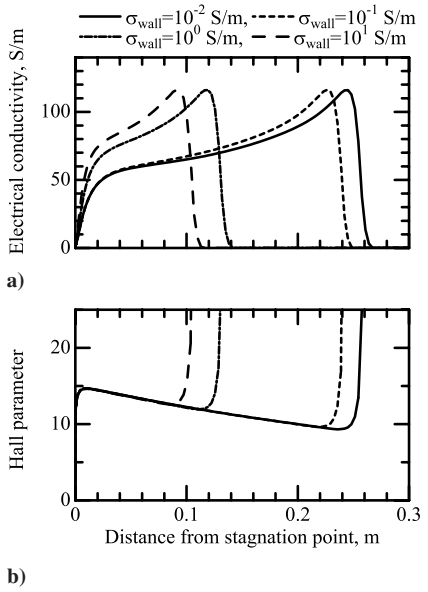

Fig. 7 Distributions of a) electrical conductivity and b) the Hall parameter in gas along the stagnation line (Δ_{wall} = 100 mm).

magnitude enough to push the shock wave cannot be obtained when the electrical conductivity of wall is more than 10^1 S/m.

Figure 9 illustrates streamlines of the electric current on the r–z plane for the electrical conductivity of wall of 10^{-1} and 10^1 S/m in the case of the wall thickness of 100 mm. The Hall effect induces the electric current density with r- and z-components as well as the azimuthal electric current density. For the electrical conductivity of wall of 10^{-1} S/m, the electric current with eddylike paths on the r–z plane does not run through the wall. The streamlines of electric current on the r–z plane for the electrical conductivity of wall of 10^{-1} S/m or less, where the shock standoff distance can be increased by applying the magnetic field, are almost the same as those for the electrical conductivity of wall of 10^{-2} S/m. These facts indicate that the effective electric resistance of wall is significantly higher than that of gas in the shock layer in the case of the electrical conductivity of wall of 10^{-1} S/m or less, and therefore there is no electrical coupling between the gas flow and the wall in the case. For the electrical conductivity of wall of 10^1 S/m, on the other hand, the electric current with eddylike paths on the r–z plane runs through the wall for the electrical conductivity of wall of 10^1 S/m, as shown in Fig. 9. The existence of paths of electric current between the gas and the wall is seen for the electrical conductivity of wall more than 10^0 S/m and becomes clearer for the electrical conductivity of wall more than 10^1 S/m, so that the strong electric field on the r–z plane cannot be obtained for the electrical conductivity of wall more than 10^1 S/m.

The aforementioned results in the case of the wall thickness of 100 mm clearly show for the first time that the upper limit of electrical conductivity of wall exists for making the MHD flow control possible and that the value of the upper limit is 10^{-1} S/m. The following briefly discusses the influence of the wall thickness on the upper limit.

The authors have found that the upper limit of electrical conductivity of wall for making the MHD flow control useful depends on the ratio of the effective electrical resistance of gas to the effective electrical resistance of wall. The effective resistance of wall is roughly in inverse proportion to the product of the electrical conductivity of wall material and the wall thickness. As shown in Fig. 5, therefore, the upper limit of electrical conductivity of wall for making the MHD flow control useful shifts to lower value in inverse proportion to the wall thickness. The values of upper limit in the cases of the wall thickness of 1, 10, and 100 mm are, respectively, 10^1, 10^0, and 10^{-1} S/m. Judging from the values of upper limit, the use of refractory ceramics [16] such as SiC ($\sigma \sim 10^{-1}$ S/m), SiO_2 ($\sigma \sim 9 \times 10^{-5}$ S/m, 773 K), and Al_2O^3 ($\sigma < 10^{-12}$ S/m) does not have problem for the usefulness of the MHD thermal protection. The refractory metals [16] such as Mo ($\sigma = 1.4 \times 10^7$ S/m, 293 K), Ti ($\sigma = 1.8 \times 10^6$ S/m, 293 K), and W ($\sigma = 1.9 \times 10^7$ S/m, 293 K), however, cannot be used as materials of wall surface.

Although only the distributions of electric potential on the r–z plane under each upper limit condition for the wall thickness wall of 1

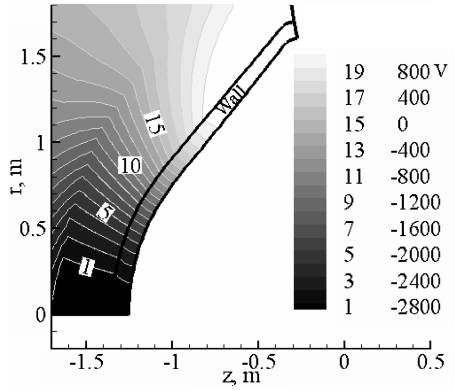

a) $\sigma_{wall} = 10^{-2}$ *S/m*

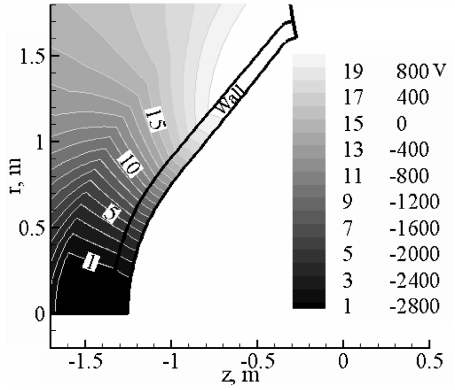

b) $\sigma_{wall} = 10^{-1}$ *S/m*

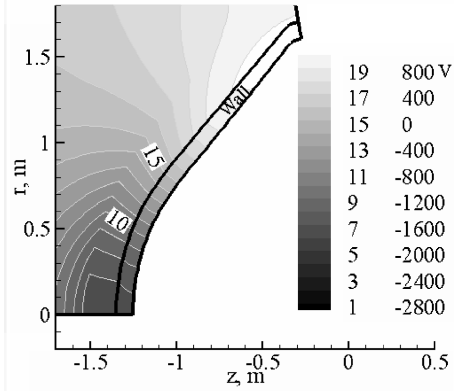

c) $\sigma_{wall} = 10^{0}$ *S/m*

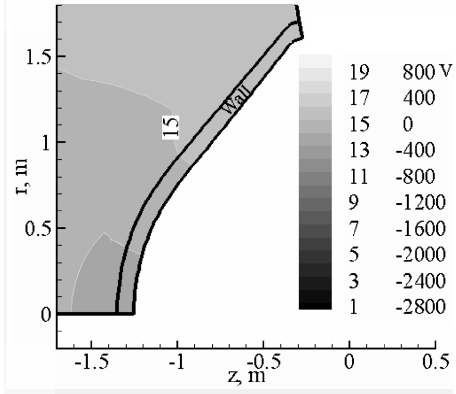

d) $\sigma_{wall} = 10^{1}$ *S/m*

Fig. 8 Distributions of electric potential ($\Delta_{wall} = 100$ mm).

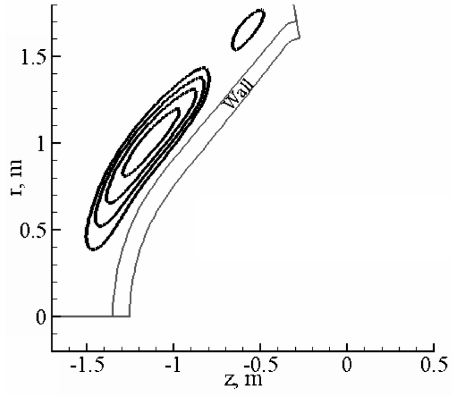

a) $\sigma_{wall} = 10^{-1}$ *S/m*

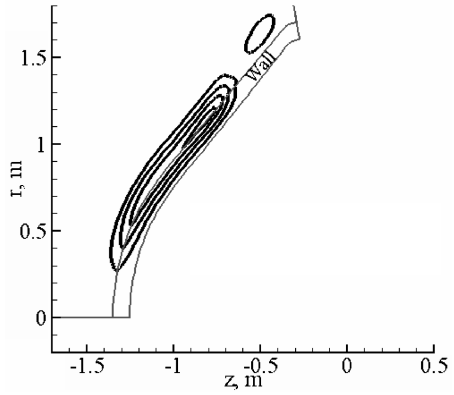

b) $\sigma_{wall} = 10^{1}$ *S/m*

Fig. 9 Distributions of electric current on the *r*–*z* plane ($\Delta_{wall} =$ 100 mm).

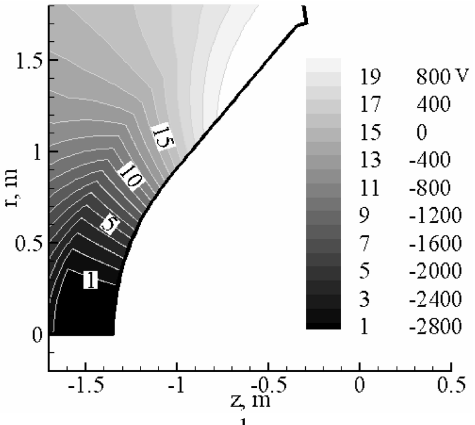

a) $\Delta_{wall} = 1$ *mm*, $\sigma_{wall} = 10^{1}$ *S/m*

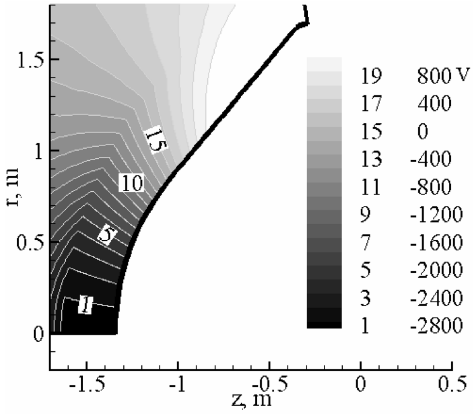

b) $\Delta_{wall} = 10$ *mm*, $\sigma_{wall} = 10^{0}$ *S/m*

Fig. 10 Distributions of electric potential in two cases.

and 10 mm are shown in Fig. 10 owing to the space limitation, the difference of the wall thickness does not significantly influence all distributions for the fluid dynamics, the electrodynamics, and the wall heat flux when the electrical conductivity of wall is the value of the upper limit or less. This is because when the electrical conductivity of wall is the value of upper limit or less, the paths of electric current between the gas and the wall do not exist for any values of wall thickness; that is, there is no electrical coupling between the gas and the wall.

IV. Conclusions

Effectiveness of the MHD flow control has been explored by the two-dimensional numerical simulations, where effects of electrical conductivity of wall of a space vehicle have been studied under the reentry flight conditions at the altitude of about 60 km in the OREX experiment for a wide range of the electrical conductivity of wall (from 10^{-5} to 10^{5} S/m) and for three different values of the wall thickness: 1, 10, and 100 mm. The results are summarized as follows:

1) It can be clearly shown for the first time that there is an upper limit of the electrical conductivity of wall for making the MHD flow control useful, and that the upper limit shifts to the lower value in inverse proportion to the wall thickness. Under the present numerical flight conditions, the values of upper limit for the wall thickness of 1, 10, and 100 mm becomes about 10^{1}, 10^{0}, and 10^{-1} S/m, respectively.

2) When the electrical conductivity of wall is the value of upper limit or less, the difference in the electrical conductivity of wall does not influence the effectiveness of the MHD flow control. This is because the paths of electric current between the gas and the wall do not exist; that is, there is no electrical coupling between the gas and the wall for any electrical conductivity of wall, when the electrical conductivity of wall is the value of upper limit or less.

Acknowledgments

This study was partly supported by University of Tsukuba Research Project. A part of computation in the present study was performed with the KDK system of Research Institute for Sustainable Humanosphere (RISH) at Kyoto University.

References

[1] Meyer, R. C., "On Reducing Aerodynamic Heat-Transfer Rates by Magnetohydrodynamic Techniques," *Journal of the Aerospace Sciences*, Vol. 25, No. 9, 1958, pp. 561–566, 572.

[2] Bush, W. B., "Magnetohydrodynamic-Hypersonic Flow Past a Blunt Body," *Journal of the Aerospace Sciences*, Vol. 25, No. 11, 1958, pp. 685–690, 728.

[3] Ziemer, R. W., "Experimental Investigation in Magneto-Aerodynamics," *ARS Journal*, Vol. 29, No. 19, 1959, pp. 642–647.

[4] Fujino, T., Funaki, I., Sugita, H., Mizuno, M., and Ishikawa, M., "Influences of Electrical Conductivity of Wall on Magnetohydrodynamic Control of Aerodynamic Heating," *Journal of Spacecraft and Rockets*, Vol. 43, No. 1, 2006, pp. 63–70.

[5] Yamamoto, Y., "Recent Comparisons of Aerothermodynamic Results by CFD and FEM Coupling Analysis with OREX Flight Experiments," *Proceedings of the 13th NAL Symposium on Aircraft Computational Aerodynamics*, National Aerospace Lab. of Japan, Tokyo, 1995, pp. 27–39.

[6] Kang, S. W., Jones, W. L., and Dunn, M. G., "Theoretical and Measured Electron-Density Distributions at High Altitudes," *AIAA Journal*, Vol. 11, No. 2, 1973, pp. 141–149.

[7] Park, C., "Assessment of Two-Temperature Kinetic Model for Ionizing Air," *Journal of Thermophysics and Heat Transfer*, Vol. 3, No. 3, 1989, pp. 233–244.

[8] Gnoffo, P. A., Gupta, R. N., and Shinn, J. L., "Conservation Equations and Physical Models for Hypersonic Air Flows in Thermal and Chemical Nonequilibrium," NASA TP-2867, Feb. 1989.

[9] Millikan, R. C., and White, D. R., "Systematics of Vibrational Relaxation," *Journal of Chemical Physics*, Vol. 39, No. 12, 1963, pp. 3209–3213.

[10] Wada, Y., and Liou, M-S., "A Flux-Splitting Scheme with High-Resolution and Robustness for Discontinuities," AIAA Paper 94-0083, Jan. 1994.

[11] Yamamoto, S., "Shock-Vortex Capturing Method and Its Application to Unsteady 3-D Cascade Flow," *Computational Fluid Dynamics Journal*, Vol. 8, No. 2, 1999, pp. 341–349.

[12] Yoon, S., and Jameson, A., "Lower-Upper Symmetric-Gauss-Seidel Method for the Euler and Navier-Stokes Equations," *AIAA Journal*, Vol. 26, No. 6, 1988, pp. 1025–1026.

[13] Fujino, T., Funaki, I., Sugita, H., Mizuno, M., and Ishikawa, M., "Numerical Analyses on Flow Control around Blunt Body 'OREX' by Magnetic Field," AIAA Paper 2003-3760, June 2003.

[14] Lobb, R. K., "Experimental Measurement of Shock Detachment Distance on Spheres Fired in Air at Hypervelocities," *The High Temperature Aspects of Hypersonic Flow*, edited by W. C. Nelson, Pergamon, New York, 1964, pp. 519–527.

[15] Yuhara, M., Fujino, T., and Ishikawa, M., "Numerical Analysis of Effects of Liquid Particles on Plasmadynamics in a Large-Scale Pulsed MHD Generator," AIAA Paper 2004-2369, June 2004.

[16] ULVAC, Inc., *Shinkuu-Handbook (Database for Vacuum Technology, in Japanese)*, 1st ed., Ohmsha, Tokyo, 2002, pp. 105–115.

A. Ketsdever
Associate Editor